

Topological boundary modes in isostatic lattices

C. L. Kane and T. C. Lubensky*

Frames, or lattices consisting of mass points connected by rigid bonds or central-force springs, are important model constructs that have applications in such diverse fields as structural engineering, architecture and materials science. The difference between the number of bonds and the number of degrees of freedom in these lattices determines the number of their zero-frequency ‘floppy modes’. When these are balanced, the system is on the verge of mechanical instability and is termed isostatic. It has recently been shown that certain extended isostatic lattices exhibit floppy modes localized at their boundary. These boundary modes are insensitive to local perturbations, and seem to have a topological origin, reminiscent of the protected electronic boundary modes that occur in the quantum Hall effect and in topological insulators. Here, we establish the connection between the topological mechanical modes and the topological band theory of electronic systems, and we predict the existence of new topological bulk mechanical phases with distinct boundary modes. We introduce one- and two-dimensional model systems that exemplify this phenomenon.

Isostatic lattices provide a useful reference point for understanding the properties of a wide range of systems on the verge of mechanical instability, including network glasses^{1,2}, randomly diluted lattices near the rigidity percolation threshold^{3,4}, randomly packed particles near their jamming threshold^{5–10}, and biopolymer networks^{11–14}. There are many periodic lattices, including the square and kagome lattices in $d = 2$ dimensions and the cubic and pyrochlore lattices in $d = 3$, that are locally isostatic with coordination number $z = 2d$ for every site under periodic boundary conditions. These lattices, which are the subject of this paper, have a surprisingly rich range of elastic responses and phonon structures^{15–19} that exhibit different behaviours as bending forces or additional bonds are added.

The analysis of such systems dates to an 1864 paper by J. C. Maxwell²⁰ that argued that a lattice with N_s mass points and N_b bonds has $N_0 = dN_s - N_b$ zero modes. Maxwell’s count is incomplete, though, because N_0 can exceed $dN_s - N_b$ if there are N_{ss} states of self-stress, where springs can be under tension or compression with no net forces on the masses. This occurs, for example, when masses are connected by straight lines of bonds under periodic boundary conditions. A more general Maxwell relation²¹,

$$\nu \equiv N_0 - N_{ss} = dN_s - N_b \quad (1)$$

is valid for infinitesimal distortions.

In a locally isostatic system with periodic boundary conditions, $N_0 = N_{ss}$. The square and kagome lattices have one state of self-stress per straight line of bonds and associated zero modes along lines in momentum space. Cutting a section of N sites from these lattices removes states of self-stress and $\mathcal{O}(\sqrt{N})$ bonds and necessarily leads to $\mathcal{O}(\sqrt{N})$ zero modes, which are essentially identical to the bulk zero modes. Rotating²² adjacent site-sharing triangles in opposite directions to create a twisted kagome lattice distorts the straight lines of bonds and removes states of self-stress. This simple modification converts lines of zero modes in the untwisted lattice to gapped modes of non-zero frequency (except for $\mathbf{q} = 0$) and localizes the required zero modes in the cut lattice to its surfaces.

These boundary zero modes are robust and insensitive to local perturbations. Boundary modes also occur in electronic systems, such as the quantum Hall effect^{23,24} and topological insulators^{25–30}.

In this paper we establish the connection between these two phenomena. Our analysis allows us to predict the existence of new topologically distinct bulk mechanical phases and to characterize the protected modes that occur on their boundary. We introduce a one-dimensional (1D) model that illustrates this phenomenon in its simplest form and maps directly to the Su–Schrieffer–Heeger (SSH) model³¹ for the electronic excitations of polyacetylene $((\text{CH}_2)_n)$, a linear polymer with alternating single and double bonds between carbon atoms (as shown in Fig. 1) that has topologically protected electron states at free ends and at interfaces. We then prove an index theorem that generalizes equation (1) and relates the local count of zero modes on the boundary to the topological structure of the bulk. We introduce a deformed version of the kagome lattice model that exhibits distinct topological phases. The predictions of an index theorem are verified explicitly by solving for the boundary modes in this model. Finally, we show that some of the distinctive features of the topological phases can be understood within a continuum elastic theory.

Mechanical modes and topological band theory

A mechanical system of masses M connected by springs with spring constant K is characterized by its equilibrium matrix²¹ Q , which relates forces $F_i = Q_{im}T_m$ to spring tensions T_m . i labels the dN_s force components on the N_s sites, and m labels the N_b bonds. Equivalently, $e_m = Q_{mi}^T u_i$ relates bond extensions e_m to site displacements u_i . The squared normal mode frequencies ω_n^2 are eigenvalues of the dynamical matrix $D = QQ^T$, where we set K/M to unity. Displacements u_i that do not lead to stretched bonds satisfy $Q^T u_i = 0$ and define the null space of Q^T , or equivalently its kernel $\ker Q^T$. The dimension of this null space $N_0 = \dim \ker Q^T$ gives the number of independent zero modes. Similarly, the null space of Q gives the $N_{ss} = \dim \ker Q$ states of self-stress. The global counts of these two kinds of zero mode are related by the rank-nullity theorem²¹, which may be expressed as an index theorem³². The index of Q , defined as $\nu = \dim \ker Q^T - \dim \ker Q$, is equal to the difference between the number of rows and columns of Q , and is given by equation (1).

At first sight, the mechanical problem and the quantum electronic problem seem different. Newton’s laws are second-order equations in time, whereas the Schrödinger equation is first order. The eigenvalues of D are positive definite, whereas an

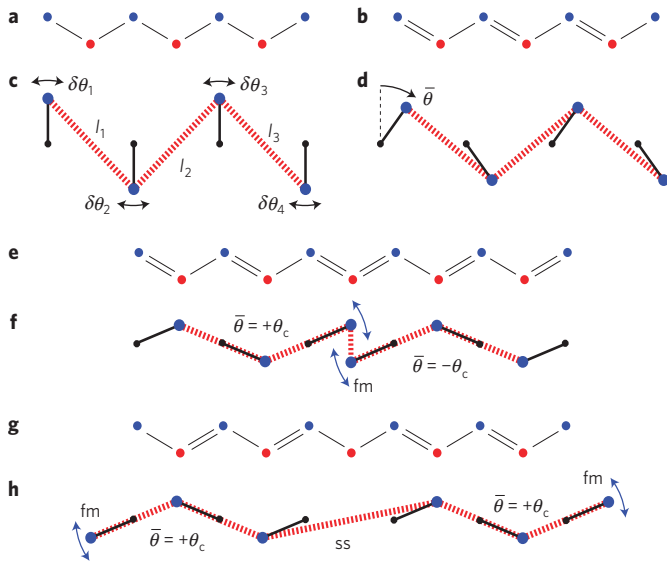


Figure 1 | 1D SSH and isostatic lattice models. **a, b**, Schematic of the SSH model of polyacetalene, with A and B sublattices indicated in blue and red. **a**, The gapless state with all bonds identical. **b**, The gapped AB dimerized state, with double (single) bonds on the AB (BA) bonds. The BA dimerized state with single and double bonds interchanged is not shown. **c, d**, The 1D isostatic lattice model in which masses, represented by the larger blue dots, are connected by springs in red and are constrained to rotate about fixed pivot points represented by small black dots. **c**, The gapless high-symmetry state with $\bar{\theta} = 0$. **d**, The gapped lower-symmetry phase with $\bar{\theta} > 0$. **c, d** are equivalent to **a, b** if we identify the masses (springs) with the A (B) sublattice sites. **e**, A domain wall in polyacetalene connecting the AB and BA dimerized states. There is a topologically protected zero-energy state associated with the A sublattice at the defect. **f**, The equivalent state for the isostatic model with a topologically protected zero-frequency floppy mode (fm) at the domain wall. **g**, Domain wall connecting the BA and AB dimerized states, which has a zero energy state associated with the B sublattice. **h**, The equivalent isostatic state with a state of self-stress (ss) at the domain wall.

electronic Hamiltonian has positive and negative eigenvalues for the conduction and valence bands. To uncover the connection between the two problems we draw our inspiration from Dirac, who famously took the ‘square root’ of the Klein–Gordon equation³³. To take the square root of the dynamical matrix, note that $D = QQ^T$ has a supersymmetric partner $\tilde{D} = Q^T Q$ with the same non-zero eigenvalues. Combining D and \tilde{D} gives a matrix that is a perfect square,

$$\mathcal{H} = \begin{pmatrix} 0 & Q \\ Q^T & 0 \end{pmatrix}; \quad \mathcal{H}^2 = \begin{pmatrix} QQ^T & 0 \\ 0 & Q^T Q \end{pmatrix} \quad (2)$$

The spectrum of \mathcal{H} is identical to that of D , except for the zero modes. Unlike D , the zero modes of \mathcal{H} include both the zero modes of Q^T and Q , which are eigenstates of $\tau^z = \text{diag}(1_{N_A}, -1_{N_B})$ distinguished by their eigenvalue, ± 1 . (Although the concept of supersymmetry is not essential for deriving this result, there is an interesting connection between the analysis leading to equation (2) and the theory of supersymmetric quantum mechanics^{34,35}.)

Viewed as a Hamiltonian, \mathcal{H} can be analysed in the framework of topological band theory²⁹. It has an intrinsic ‘particle–hole’ symmetry, $\{\mathcal{H}, \tau^z\} = 0$, which guarantees eigenstates come in $\pm E$ pairs. As Q_{im} is real, $\mathcal{H} = \mathcal{H}^*$ has ‘time-reversal’ symmetry. These define symmetry class BDI (ref. 36). In one-dimension, gapped Hamiltonians in this class, such as the SSH model, are characterized by an integer topological invariant $n \in \mathbb{Z}$ that is a property of the Bloch Hamiltonian $\mathcal{H}(k)$ (or equivalently $Q(k)$) defined at each

wavenumber k in the Brillouin zone. A mapping of $\mathcal{H}(k)$ to the complex plane is provided by $\det Q(k) = |\det Q(k)|e^{i\phi(k)}$. If bulk modes are all gapped then $|\det Q(k)|$ is non-zero and $Q(k) \in GL_p$, where p is the dimension of $Q(k)$. $Q(k)$ is then classified by the integer winding number of $\phi(k)$ around the Brillouin zone: $\phi(k+G) - \phi(k) = 2\pi n$, where G is a reciprocal lattice vector, which defines an element of the homotopy group $\pi_1(GL_p) = \mathbb{Z}$. A consequence is that a domain wall across which n changes is associated with topologically protected zero modes^{31,37,38}. Below, we present an index theorem that unifies this bulk–boundary correspondence with equation (1) and shows how it can be applied to d -dimensional lattices, which form the analogue of weak topological insulators²⁸.

Topological edge modes have been previously predicted in 2D photonic^{39,40} and phononic⁴¹ systems. These differ from the present theory because they occur in systems with bandgaps at finite frequency and broken time-reversal symmetry (symmetry class A). Localized end modes were found in a time-reversal invariant 1D model (class AI; ref. 42). However, the presence of those finite frequency modes is not topologically guaranteed.

1D model

Before discussing the index theorem we introduce a simple 1D elastic model, equivalent to the SSH model, that illustrates the topological modes in their simplest setting. Consider a 1D system of springs connecting masses constrained to rotate at a radius R about fixed pivot points. In Fig. 1c the spring lengths are set so that the equilibrium configuration is $\langle \theta_i \rangle = 0$. Figure 1d shows a configuration with shorter springs with $\langle \theta_i \rangle = \bar{\theta}$. Expanding in deviations $\delta\theta_i$ about $\bar{\theta}$, the extension of spring m is $\delta\ell_m = Q_{mi}^T \delta\theta_i$, with $Q_{mi}^T = q_1(\bar{\theta})\delta_{m,i} + q_2(\bar{\theta})\delta_{m,i+1}$ and

$$q_{1(2)} = r \cos \bar{\theta} (r \sin \bar{\theta} \pm 1) / \sqrt{4r^2 \cos^2 \bar{\theta} + 1}$$

The normal mode dispersion is $\omega(k) = |Q(k)|$, where $Q(k) = q_1 + q_2 e^{ik}$. When $\bar{\theta} = 0$, $q_1 = -q_2$, and there are gapless bulk modes near $k=0$. For a finite system with N sites and $N-1$ springs, there are no states of self-stress and only a single extended zero mode, as required by equation (1). For $\bar{\theta} \neq 0$ the bulk spectrum has a gap. In this case, the zero mode required by equation (1) is localized at one end or the other, depending on the sign of $\bar{\theta}$. The $\bar{\theta} > 0$ and $\bar{\theta} < 0$ phases are topologically distinct in the sense that it is impossible to tune between the two phases without passing through a transition where the gap vanishes. The topological distinction is captured by the winding number of the phase of $Q(k)$, which is 1 (0) for $|q_1| < (>) |q_2|$.

Viewed as a quantum Hamiltonian, equation (2) for this model is identical to the SSH model³¹, as indicated in Fig. 1a,b. The sites and the bonds correspond, respectively, to the A and B sublattices of the SSH model. For $\bar{\theta} = 0$ the bonds in the SSH model are the same (Fig. 1a), whereas for $\bar{\theta} \neq 0$ they are dimerized (Fig. 1b). The two topological phases correspond to the two dimerization patterns for polyacetalene. As is well known for the SSH model^{31,37}, an interface between the two dimerizations binds a zero mode, as indicated in Fig. 1e,g. This is most easily seen for $\bar{\theta} = \pm\theta_c$ where the springs are colinear with the bars, so that q_1 or $q_2 = 0$. Figure 1f shows a domain wall between $+\theta_c$ and $-\theta_c$, in which the centre two sites share a localized floppy mode. Figure 1h shows an interface between $-\theta_c$ and $+\theta_c$ with a state of self-stress localized to the middle three bonds, in addition to floppy modes localized at either end. As long as there is a bulk gap, the zero modes cannot disappear when $\bar{\theta}$ deviates from $\pm\theta_c$. The zero modes remain exponentially localized, with a localization length that diverges when $\bar{\theta} \rightarrow 0$.

Index theorem

There seem to be two distinct origins for zero modes. In equation (1) they arise because of a mismatch between the number

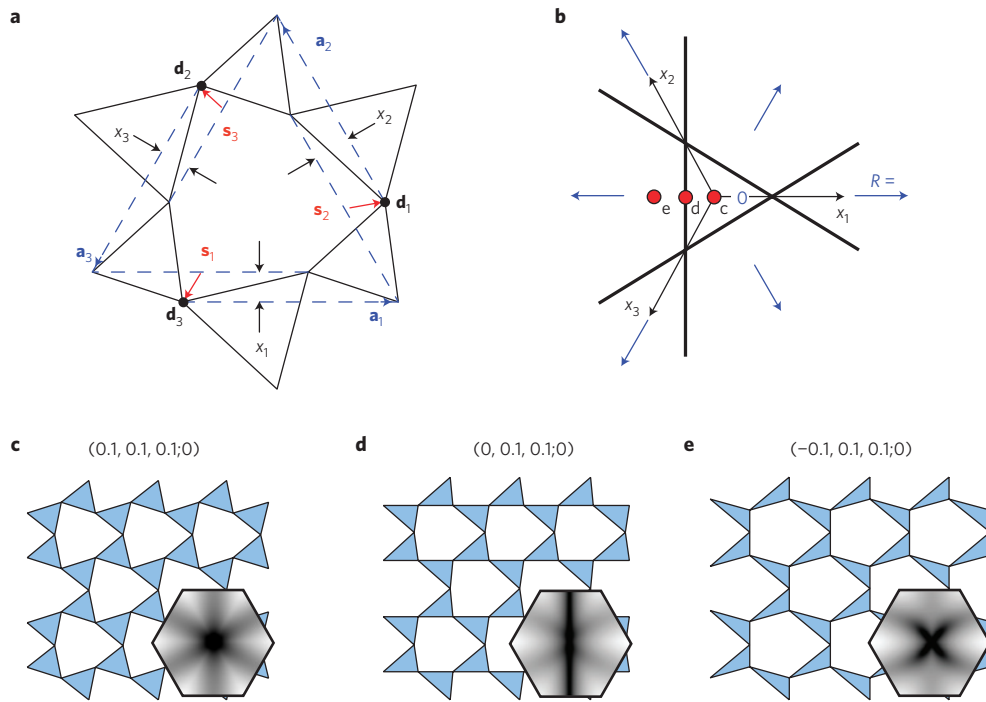


Figure 2 | Deformed kagome lattice model. **a**, Our convention for labelling the states. **b**, A ternary plot of the phase diagram for fixed $x_1 + x_2 + x_3 > 0$. The phases are labelled by \mathbf{R} , which is zero in the central phase and a nearest-neighbour lattice vector in the other phases. The red circles indicate lattices shown in panels **c–e**. **c–e**, Representative structures for $\mathbf{R} = 0$ (**c**) and $\mathbf{R} \neq 0$ (**e**) and the transition between them (**d**). The insets are density plots of the smallest mode frequency as a function of \mathbf{k} in the Brillouin zone. In **c** the gap vanishes only at $\mathbf{k} = 0$, whereas in **d** it vanishes on the line $k_x = 0$. **e**, The gap vanishes only at $\mathbf{k} = 0$, but has a quadratic dependence in some directions for small \mathbf{k} .

of sites and bonds, whereas at a domain wall they arise in a location where there is no local mismatch. To unify them, we generalize the index theorem so that it determines the zero-mode count ν^S in a subsystem S of a larger system. This is well defined provided the boundary of S is deep in a gapped phase where zero modes are absent. We will show that there are two contributions,

$$\nu^S = \nu_L^S + \nu_T^S \quad (3)$$

where ν_L^S is a local count of sites and bonds in S and ν_T^S is a topological count, which depends on the topological structure of the gapped phases on the boundary of S .

To prove equation (3) and to derive formulas for ν_T^S and ν_L^S , we adapt a local version of the Callias index theorem^{43–46} to allow for the possibility of non-zero ν_L^S . The details of the proof are given in the Supplementary Information. Here we will focus on the results. Consider a d -dimensional system described by a Hamiltonian matrix $\mathcal{H}_{\alpha\beta}$, where α labels a site or a bond centred on \mathbf{r}_α . The count of zero modes in S may be written

$$\nu^S = \lim_{\epsilon \rightarrow 0} \text{Tr} \left[\tau^z \rho_S(\mathbf{r}) \frac{i\epsilon}{\mathcal{H} + i\epsilon} \right] \quad (4)$$

where $\mathbf{r}_{\alpha\beta} = \delta_{\alpha\beta} \mathbf{r}_\alpha$. The region S is defined by the support function $\rho^S(\mathbf{r}) = 1$ for $\mathbf{r} \in S$ and 0 otherwise. It is useful to consider $\rho^S(\mathbf{r})$ to vary smoothly between 1 and 0 on the boundary ∂S . Expanding the trace in terms of eigenstates of \mathcal{H} shows that only zero modes with support in S contribute.

In the Supplementary Information we show that equation (4) can be rewritten as equation (3) with

$$\nu_L^S = \text{Tr}[\rho^S(\mathbf{r}) \tau^z] \quad (5)$$

and

$$\nu_T^S = \int_{\partial S} \frac{d^{d-1}S}{V_{\text{cell}}} \mathbf{R}_T \cdot \hat{n} \quad (6)$$

where the integral is over the boundary of S with inward-pointing normal \hat{n} . $\mathbf{R}_T = \sum_i n_i \mathbf{a}_i$ is a Bravais lattice vector characterizing the periodic crystal in the boundary region that can be written in terms of primitive vectors \mathbf{a}_i and integers

$$n_i = \frac{1}{2\pi i} \oint_{C_i} d\mathbf{k} \cdot \text{Tr}[Q(\mathbf{k})^{-1} \nabla_{\mathbf{k}} Q(\mathbf{k})] = \frac{1}{2\pi} \oint_{C_i} d\mathbf{k} \cdot \nabla_{\mathbf{k}} \phi(\mathbf{k}) \quad (7)$$

Here C_i is a cycle of the Brillouin zone connecting \mathbf{k} and $\mathbf{k} + \mathbf{b}_i$, where \mathbf{b}_i is a primitive reciprocal vector satisfying $\mathbf{a}_i \cdot \mathbf{b}_j = 2\pi \delta_{ij}$. n_i are winding numbers of the phase of $\det Q(\mathbf{k})$ around the cycles of the Brillouin zone, where $Q(\mathbf{k})$ is the equilibrium matrix in a Bloch basis.

To apply equations (6) and (7), it is important that the winding number be independent of path. This is the case if there is a gap in the spectrum. We will also apply this when the gap vanishes for acoustic modes at $\mathbf{k} = 0$. This is okay because the acoustic mode is not topological in the sense that it can be gapped by a weak translational-symmetry-breaking perturbation. This means that the winding number is independent of \mathbf{k} even near $\mathbf{k} = 0$. It is possible, however, that there can be topologically protected gapless points. These would be point zeros around which the phase of $\det Q(\mathbf{k})$ advances by 2π . These lead to topologically protected bulk modes that form the analogue of a ‘Dirac semimetal’ in electronic systems such as graphene. These singularities could be of interest, but they do not occur in the model we study below.

A second caveat for equation (7) is that, in general, the winding number is not gauge invariant and depends on how the sites

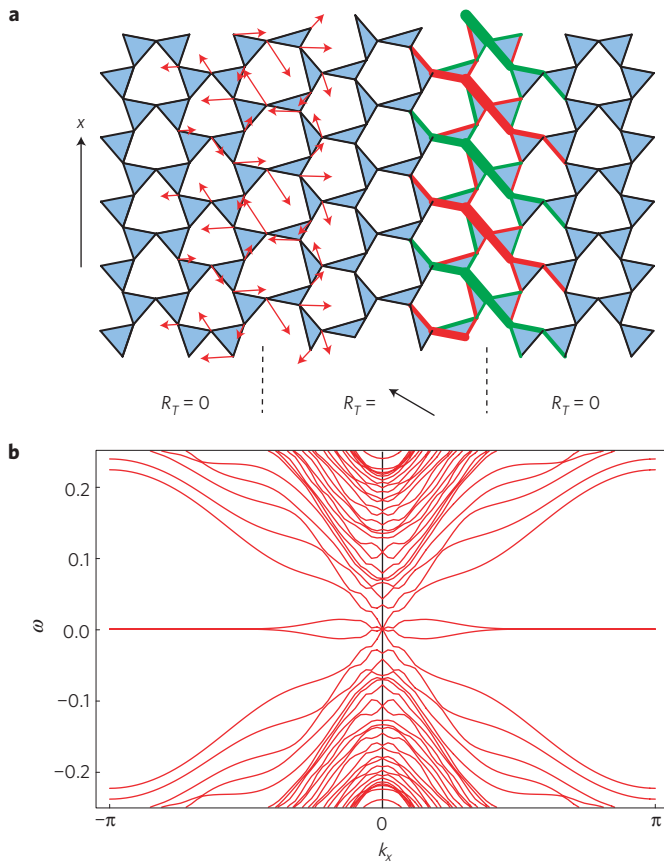


Figure 3 | Zero modes at domain walls. **a**, A lattice with periodic boundary conditions and two domain walls, the left one between $(0.1, 0.1, 0.1, 0)$ and $(0.1, 0.1, -1, 0)$ with zero modes and the right one between $(0.1, 0.1, -1, 0)$ and $(0.1, 0.1, +0.1, 0)$ with states of self-stress. The zero-mode eigenvectors at $k_x = \pi$ are indicated for the floppy mode (arrows) and the state of self-stress (red (+) and green (-) thickened bonds). **b**, The vibrational mode dispersion as a function of k_x .

and bonds are assigned to unit cells. In the Supplementary Information we show that for an isostatic lattice with uniform coordination it is possible to adopt a ‘standard unit cell’ with basis vectors $\mathbf{d}_{i(m)}$ for the n_s sites (dn_s bonds) per cell that satisfy $\mathbf{r}_0 = d \sum_i \mathbf{d}_i - \sum_m \mathbf{d}_m = 0$. $Q(\mathbf{k})$ is defined using Bloch basis states $|\mathbf{k}, a = i, m\rangle \propto \sum_{\mathbf{R}} \exp(i\mathbf{k} \cdot (\mathbf{R} + \mathbf{d}_a)) |\mathbf{R} + \mathbf{d}_a\rangle$, where \mathbf{R} is a Bravais lattice vector. In this gauge, \mathbf{R}_T is uniquely defined and the zero-mode count is given by equations (3) and (5)–(7).

To determine the number of zero modes per unit cell on an edge indexed by a reciprocal lattice vector \mathbf{G} , consider a cylinder with axis parallel to \mathbf{G} and define the region S to be the points nearest to one end of the cylinder (see Supplementary Fig. 1). v_T^S is determined by evaluating equation (6), with the aid of equation (7) on ∂S deep in the bulk of the cylinder. It follows that

$$\bar{v}_T \equiv v_T^S / N_{\text{cell}} = \mathbf{G} \cdot \mathbf{R}_T / 2\pi \quad (8)$$

The local count, v_T^S , depends on the details of the termination at the surface and can be determined by evaluating the macroscopic ‘surface charge’ that arises when charges $+d$ (-1) are placed on the sites (bonds) in a manner analogous to the ‘pebble game’⁴. This can be found by defining a bulk unit cell with basis vectors \mathbf{d}_a that accommodates the surface with no leftover sites or bonds (see Fig. 4a below). Note that this unit cell depends on the surface termination and, in general, will be different from the

‘standard’ unit cell used for v_T^S . The local count is then the surface polarization charge given by the dipole moment per unit cell. We find

$$\bar{v}_T \equiv v_T^S / N_{\text{cell}} = \mathbf{G} \cdot \mathbf{R}_L / 2\pi \quad (9)$$

where

$$\mathbf{R}_L = d \sum_{\text{sites } i} \mathbf{d}_i - \sum_{\text{bonds } m} \mathbf{d}_m \quad (10)$$

\mathbf{R}_L is similar to \mathbf{r}_0 defined above (which is assumed to be zero), but it is in general a different Bravais lattice vector. The total zero mode count on the surface then follows from equations (3), (8) and (9).

Deformed kagome lattice model

We now illustrate the topological boundary modes of a 2D lattice with the connectivity of the kagome lattice, but with deformed positions. The deformed kagome lattice is specified by its Bravais lattice and basis vectors for the three atoms per unit cell. For simplicity, we fix the Bravais lattice to be hexagonal with primitive vectors $\mathbf{a}_{p+1} = (\cos 2\pi p/3, \sin 2\pi p/3)$. We parameterize the basis vectors as $\mathbf{d}_1 = \mathbf{a}_1/2 + \mathbf{s}_2$, $\mathbf{d}_2 = \mathbf{a}_2/2 - \mathbf{s}_1$ and $\mathbf{d}_3 = \mathbf{a}_3/2$. Defining $\mathbf{s}_3 = -\mathbf{s}_1 - \mathbf{s}_2$, \mathbf{s}_p describe the displacement of \mathbf{d}_{p-1} relative to the midpoint of the line along \mathbf{a}_p that connects its neighbours at $\mathbf{d}_{p+1} \pm \mathbf{a}_{p\mp 1}$ (with p defined mod 3), as indicated in Fig. 2a. \mathbf{s}_p are specified by 6 parameters with 2 constraints. A symmetrical representation is to take $\mathbf{s}_p = x_p(\mathbf{a}_{p-1} - \mathbf{a}_{p+1}) + y_p \mathbf{a}_p$ and to use independent variables $(x_1, x_2, x_3; z)$ with $z = y_1 + y_2 + y_3$. The constraints then determine $y_p = z/3 + x_{p-1} - x_{p+1}$. x_p describes the buckling of the line of bonds along \mathbf{a}_p , so that when $x_p = 0$ the line of bonds is straight. z describes the asymmetry in the sizes of the two triangles. $(0, 0, 0; 0)$ is the undistorted kagome lattice, and $(x, x, x; 0)$ is the twisted kagome lattice, studied in ref. 22, with twist angle $\theta = \tan^{-1}(2\sqrt{3}x)$.

It is straightforward to solve for the bulk normal modes of the periodic lattice. When any of the x_p are zero the gap vanishes on the line $\mathbf{k} \cdot \mathbf{a}_p = 0$ in the Brillouin zone. This line of zero modes is a special property of this model that follows from the presence of straight lines of bonds along \mathbf{a}_p . When $x_p = 0$ the system is at a critical point separating topologically distinct bulk phases. The phase diagram features the eight octants specified by the signs of $x_{1,2,3}$. $(+++)$ and $(---)$ describe states, topologically equivalent to the twisted kagome lattice, with $\mathbf{R}_T = 0$. The remaining 6 octants are states that are topologically distinct, but are related to each other by C_6 rotations. We find that

$$\mathbf{R}_T = \sum_{p=1}^3 \mathbf{a}_p \text{sgn} x_p / 2 \quad (11)$$

is independent of z . Figure 2b shows a ternary plot of the phase diagram as a function of x_1, x_2, x_3 for $z = 0$ and a fixed value of $x_1 + x_2 + x_3$. Figure 2c–e shows representative structures for the $\mathbf{R}_T = 0$ phase (Fig. 2c), the $\mathbf{R}_T \neq 0$ phase (Fig. 2e), and the transition between them (Fig. 2d). The insets show density plots of the lowest frequency mode, which highlight the gapless point due to the acoustic mode in Fig. 2c and the gapless line due to states of self-stress in Fig. 2d. In Fig. 2e, the gap vanishes only at the origin, but the cross arises because acoustic modes vary quadratically rather than linearly with \mathbf{k} along its axes. This behaviour will be discussed in the next section.

We next examine the boundary modes of the deformed kagome lattice. Figure 3 shows a system with periodic boundary conditions in both directions, which has domain walls separating $(0.1, 0.1, 0.1; 0)$ from $(0.1, 0.1, -0.1; 0)$. As there are no broken

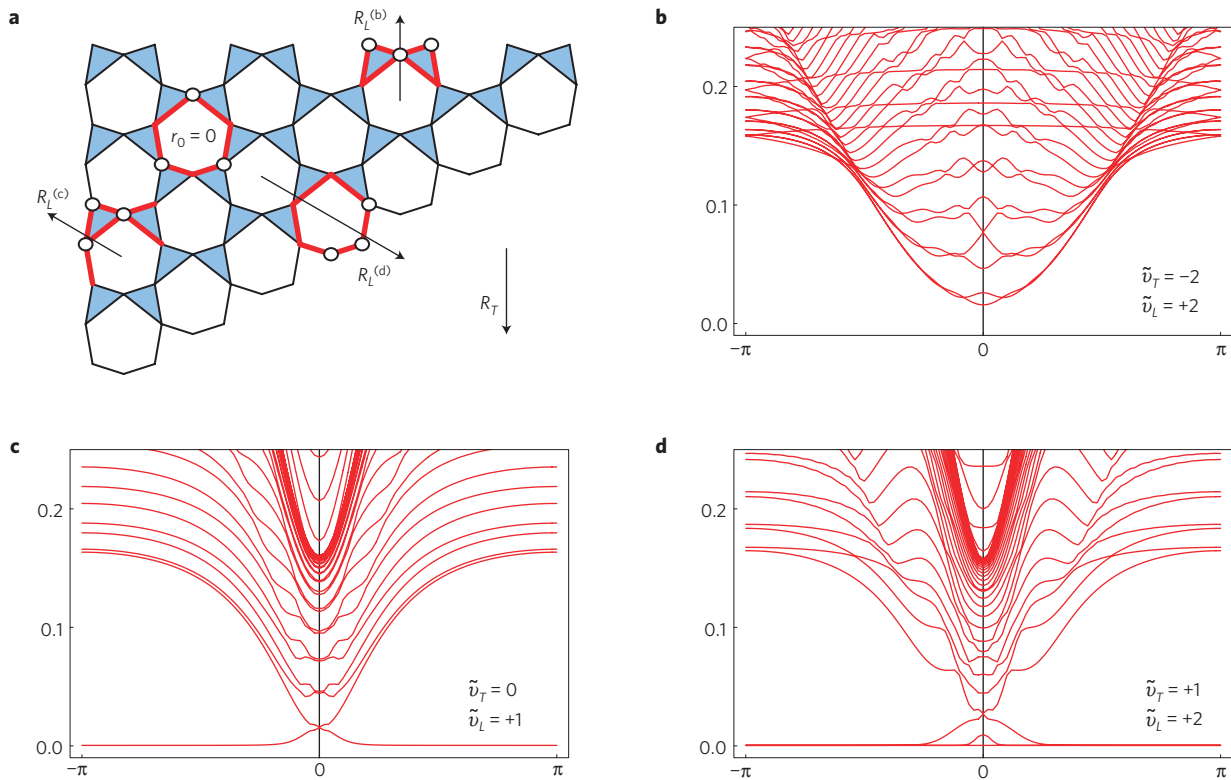


Figure 4 | Zero modes at the edge. **a**, A $(-0.05, 0.05, 0.05, 0)$ lattice indicating three edges, superscript letters indicate panels **b–d**. **b–d**, The vibrational mode spectrum computed for a strip with one edge as shown in **a** and the other edge with a clamped boundary condition. The zero-mode count on each surface is compared with equations (3), (8) and (9).

bonds, the local count is $v_S^L = 0$. On the two domain walls, equation (8) predicts

$$\tilde{v}_T = \mathbf{G} \cdot (\mathbf{R}_T^1 - \mathbf{R}_T^2) = +1(-1) \quad (12)$$

for the left (right) domain wall, where \mathbf{R}_T^1 and \mathbf{R}_T^2 characterize the material to the left and right of the domain wall, respectively (see Supplementary Fig. 1). Note that the indices of the two domain walls are opposite in sign so that the total index ν of equation (1) is zero as required. Figure 2c shows the spectrum of \mathcal{H} (which has both positive and negative eigenvalues) as a function of the momentum k_x parallel to the domain wall. The zero modes of \mathcal{H} include both the floppy modes and the states of self-stress. In the vicinity of $k_x = 0$ the zero modes on the two domain walls couple and split because their penetration depth diverges as $k_x \rightarrow 0$. The eigenvectors for the zero modes at $k_x = \pi$ are indicated in Fig. 3a by the arrows and the thickened bonds.

Figure 4a shows a segment of a $(-0.05, 0.05, 0.05, 0)$ lattice with three different different edges. For each edge, a unit cell that accommodates the edge is shown, along with the corresponding \mathbf{R}_L , from which \tilde{v}_L is determined. In the interior, a ‘standard’ unit cell, with $\mathbf{r}_0 = 0$ is shown. Figure 4b–d shows the spectrum for a strip with one edge given by the corresponding edge in Fig. 4a with free boundary conditions. The other edge of the strip is terminated with clamped boundary conditions, so that the floppy modes are due solely to the free edge. The number of zero modes per unit cell agrees with equations (8) and (9) for each surface given \mathbf{R}_L and \mathbf{R}_T . The zero modes acquire a finite frequency when the penetration length of the zero mode approaches the strip width, which leads to Gaussian ‘bumps’ near $k = 0$, which will be discussed in the next section. In Fig. 4d, one of the three zero modes can be identified as a

localized ‘rattler’, which remains localized on the surface sites, even for $k \rightarrow 0$.

Continuum elasticity theory

Unlike electronic spectra, phonon spectra have acoustic modes whose frequencies vanish as $\mathbf{k} \rightarrow 0$. These excitations along with macroscopic elastic distortions and long-wavelength surface Rayleigh waves are described by a continuum elastic energy quadratic in the elastic strain tensor u_{ij} . Elastic energies are restricted to small wavenumber and cannot by themselves determine topological characteristics, such as those we are considering, that depend on properties across the Brillouin zone. Nevertheless, the elastic energies of our model isostatic lattices fall into distinct classes depending on the topological class of the lattice. For simplicity we focus on $(x_1, x_2, x_2; 0)$ states, where $x_2 > 0$ is fixed and x_1 is allowed to vary. The elastic energy density f can be written as

$$f = \frac{K}{2} [(u_{xx} - a_1 u_{yy})^2 + 2a_4 u_{xy}^2] \quad (13)$$

We find that $a_1 \propto x_1$ for small x_1 , whereas $a_4 > 0$ and K are positive and smoothly varying near $x_1 = 0$. Thus, the $\mathbf{R}_T = 0$ and $\mathbf{R}_T \neq 0$ sectors are distinguished by the sign of a_1 . $f = 0$ for shape distortions with $u_{xx} = a_1 u_{yy}$ and $u_{xy} = 0$. When $a_1 > 0$, the distortion has a negative Poisson ratio⁴⁷, expanding or contracting in orthogonal directions (a feature shared by the twisted kagome lattice²²); when $a_1 < 0$, the distortion has the more usual positive Poisson ratio. Finally, when $a_1 = 0$, uniaxial compressions along y costs no energy.

Expanding $\det Q^T$ for small \mathbf{k} provides useful information about the bulk- and surface-mode structure. To order k^3 ,

$$\det Q^T = A[k_x^2 + a_1 k_y^2 + ic(k_x^3 - 3k_x k_y^2)] + O(k^4) \quad (14)$$

where $A, c > 0$ for small x_1 . a_1 is the same as in equation (13). Long-wavelength zero modes are solutions of $\det Q^T = 0$. The quadratic term, which corresponds to the elastic theory, equation (13), reveals an important difference between the bulk acoustic modes of $R_T = 0$ and $R_T \neq 0$. In the former case, $a_1 > 0$, $\det Q^T = 0$ only at $\mathbf{k} = 0$. For $a_1 < 0$, though, to order k^2 , $\det Q^T = 0$ for $k_x = \pm \sqrt{|a_1|} k_y$, so the elastic theory predicts lines of gapless bulk modes. The degeneracy is lifted by the k^3 term, leading to a k^2 dispersion along those lines, which can be seen by the cross in the density map of Fig. 2e.

$\det Q^T(\mathbf{k} \rightarrow 0)$ vanishes for complex wavenumbers associated with zero-frequency Rayleigh surface waves. Writing $\mathbf{k} = k_\perp \hat{n} + k_\parallel \hat{z} \times \hat{n}$ for a surface whose outward normal \hat{n} makes an angle θ with \hat{x} , there is an $\omega = 0$ Rayleigh wave with penetration depth $|\text{Im } k_\perp|^{-1}$ if $\text{Im } k_\perp < 0$. To order k_\parallel^2 there are two solutions,

$$k_\perp^\pm = \frac{\sin \theta \pm i\sqrt{a_1} \cos \theta}{\cos \theta \mp i\sqrt{a_1} \sin \theta} k_\parallel + \frac{i(3+a_1)d}{2(\cos \theta \pm i\sqrt{a_1} \sin \theta)^3} k_\parallel^2 \quad (15)$$

When $a_1 > 0$, the linear term is always finite and non-zero, and $\text{Im } k_\perp^\pm$ have opposite signs, indicating that there can be acoustic surface zero modes on all surfaces. These are the classical Rayleigh waves predicted by the elastic theory, with penetration depth $\mathcal{O}(k_\parallel^{-1})$. When $a_1 < 0$, the linear term in k_\parallel is real and $\text{Im } k_\perp^\pm \propto k_\parallel^2$. The number of long-wavelength surface zero modes depends on the angle of the surface. When $|\theta| < \theta_c = \cot^{-1} \sqrt{|a_1|}$, $\text{Im } k_\perp^\pm$ are both positive, and there are no acoustic surface zero modes. The opposite surface, $|\theta - \pi| < \theta_c$, has two acoustic surface modes. For $\theta_c < \theta < \pi - \theta_c$, $\text{Im } k_\perp^\pm$ have opposite signs, so there is one mode. This is consistent with the mode structure in Fig. 4. The $\mathcal{O}(k_\parallel^{-2})$ penetration depth explains the Gaussian profile of the $k \rightarrow 0$ bumps in the zero modes, which are due to the finite strip width. In Fig. 4b, a $\theta = 0$ surface has no zero modes. Figure 4c shows a $\theta = \pi/2 > \theta_c$ surface with one long-wavelength surface zero mode. Figure 4d shows the spectrum with $\pi - \theta = \pi/6 < \theta_c$ with two bumps indicating two deeply penetrating long-wavelength zero modes in addition to one non-acoustic mode localized at that surface.

Conclusions

We have developed a general theory of topological phases of isostatic lattices, which explains the boundary zero modes and connects to the topological band theory of electronic systems. This points to several directions for future studies. It will be interesting to study 3D lattice models, as well as lattices that support point singularities in $\det Q(\mathbf{k})$ analogous to Dirac semimetals. Finally, it will be interesting to explore connections with theories of frustrated magnetism⁴⁸.

Received 2 August 2013; accepted 12 November 2013;
published online 8 December 2013

References

- Phillips, J. C. Topology of covalent non-crystalline solids 2. medium-range order in chalcogenide alloys and α -Si(Ge). *J. Non-Cryst. Solids* **43**, 37–77 (1981).
- Thorpe, M. F. Continuous deformations in random networks. *J. Non-Cryst. Solids* **57**, 355–370 (1983).
- Feng, S. & Sen, P. N. Percolation on elastic networks—new exponent and threshold. *Phys. Rev. Lett.* **52**, 216–219 (1984).
- Jacobs, D. J. & Thorpe, M. F. Generic rigidity percolation—the pebble game. *Phys. Rev. Lett.* **75**, 4051–4054 (1995).
- Liu, A. J. & Nagel, S. R. Nonlinear dynamics—Jamming is not just cool any more. *Nature* **396**, 21–22 (1998).
- Liu, A. J. & Nagel, S. R. Granular and jammed materials. *Soft Matter* **6**, 2869–2870 (2010).
- Liu, A. J. & Nagel, S. R. The jamming transition and the marginally jammed solid. *Annu. Rev. Condens. Matter Phys.* **1**, 347–369 (2010).
- Torquato, S. & Stillinger, F. H. Jammed hard-particle packings: From Kepler to Bernal and beyond. *Rev. Mod. Phys.* **82**, 2633–2672 (2010).
- Wyart, M., Nagel, S. R. & Witten, T. A. Geometric origin of excess low-frequency vibrational modes in weakly connected amorphous solids. *Europhys. Lett.* **72**, 486–492 (2005).
- Wyart, M. On the rigidity of amorphous solids. *Ann. De Phys.* **30**, 1–96 (2005).
- Wilhelm, J. & Frey, E. Elasticity of stiff polymer networks. *Phys. Rev. Lett.* **91**, 108103 (2003).
- Heussinger, C. & Frey, E. Floppy modes and nonaffine deformations in random fibre networks. *Phys. Rev. Lett.* **97**, 105501 (2006).
- Huisman, L. & Lubensky, T. C. Internal stresses, normal modes and non-affinity in three-dimensional biopolymer networks. *Phys. Rev. Lett.* **106**, 088301 (2011).
- Broedersz, C., Mao, X., Lubensky, T. C. & MacKintosh, F. C. Criticality and isostaticity in fibre networks. *Nature Phys.* **7**, 983–988 (2011).
- Souslov, A., Liu, A. J. & Lubensky, T. C. Elasticity and response in nearly isostatic periodic lattices. *Phys. Rev. Lett.* **103**, 205503 (2009).
- Mao, X. M., Xu, N. & Lubensky, T. C. Soft modes and elasticity of nearly isostatic lattices: Randomness and dissipation. *Phys. Rev. Lett.* **104**, 085504 (2010).
- Mao, X. M. & Lubensky, T. C. Coherent potential approximation of random nearly isostatic kagome lattice. *Phys. Rev. E* **83**, 011111 (2011).
- Mao, X. M., Stenull, O. & Lubensky, T. C. Elasticity of a filamentous kagome lattice. *Phys. Rev. E* **87**, 042602 (2013).
- Kapko, V., Treacy, M. M. J., Thorpe, M. F. & Guest, S. D. On the collapse of locally isostatic networks. *Proc. R. Soc. A* **465**, 3517–3530 (2009).
- Maxwell, J. C. On the calculation of the equilibrium stiffness of frames. *Phil. Mag.* **27**, 294–299 (1865).
- Calladine, C. R. Buckminster Fuller's 'tensegrity' structures and clerk Maxwell's rules for the construction of stiff frames. *Int. J. Solids Struct.* **14**, 161–172 (1978).
- Sun, K., Mao, X. & Lubensky, T. C. Surface phonons, elastic response, and conformal invariance in twisted kagome lattices. *Proc. Natl Acad. Sci. USA* **109**, 12369–12374 (2012).
- Halperin, B. I. Quantized hall conductance, current-carrying edge states, and the existence of extended states in a two-dimensional disordered potential. *Phys. Rev. B* **25**, 2185–2190 (1982).
- Haldane, F. D. M. Model for a quantum hall effect without landau levels—condensed matter realization of the parity anomaly. *Phys. Rev. Lett.* **61**, 2015–2018 (1988).
- Kane, C. L. & Mele, E. J. Z(2) topological order and the quantum spin Hall effect. *Phys. Rev. Lett.* **95**, 146802 (2005).
- Bernevig, B. A., Hughes, T. L. & Zhang, S.-C. Quantum spin hall effect and topological phase transition in HgTe quantum wells. *Science* **314**, 1757–1761 (2006).
- Moore, J. E. & Balents, L. Topological invariants of time-reversal-invariant band structures. *Phys. Rev. B* **75**, 121306 (2007).
- Fu, L., Kane, C. L. & Mele, E. J. Topological insulators in three dimensions. *Phys. Rev. Lett.* **98**, 106803 (2007).
- Hasan, M. Z. & Kane, C. L. Colloquium: Topological insulators. *Rev. Mod. Phys.* **82**, 3045–3067 (2010).
- Qi, X.-L. & Zhang, S.-C. Topological insulators and superconductors. *Rev. Mod. Phys.* **83**, 1057–1110 (2011).
- Su, W. P., Schrieffer, J. R. & Heeger, A. J. Solitons in polyacetalene. *Phys. Rev. Lett.* **42**, 1698 (1979).
- Nakahara, M. *Geometry, Topology and Physics* (Hilger, 1990).
- Dirac, P. A. M. The quantum theory of the electron. *R. Soc. Lond. Proc. A* **117**, 610–624 (1928).
- Witten, E. Dynamical breaking of supersymmetry. *Nucl. Phys. B* **188**, 513–554 (1981).
- Cooper, F., Khare, A. & Sukhatme, U. Supersymmetry and quantum mechanics. *Phys. Rep.* **251**, 267–385 (1995).
- Schnyder, A. P., Ryu, S., Furusaki, A. & Ludwig, A. W. W. Classification of topological insulators and superconductors in three spatial dimensions. *Phys. Rev. B* **78**, 195125 (2008).
- Jackiw, R. & Rebbi, C. Solitons with fermion number 1/2. *Phys. Rev. D* **13**, 3398–3409 (1976).
- Volovik, G. E. *The Universe in a Helium Droplet* (Clarendon, 2003).
- Haldane, F. D. M. & Raghun, S. Possible realization of directional optical waveguides in photonic crystals with broken time-reversal symmetry. *Phys. Rev. Lett.* **100**, 013904 (2008).
- Wang, Z., Chong, Y. D., Joannopoulos, J. D. & Soljačić, M. Reflection-free one-way edge modes in a gyromagnetic photonic crystal. *Phys. Rev. Lett.* **100**, 013905 (2008).
- Prodan, E. & Prodan, C. Topological phonon modes and their role in dynamic instability of microtubules. *Phys. Rev. Lett.* **103**, 248101 (2009).
- Berg, N., Joel, K., Kooyk, M. & Prodan, E. Topological phonon modes in filamentary structures. *Phys. Rev. E* **83**, 021913 (2011).
- Callias, C. Axial anomalies and index theorems on open spaces. *Commun. Math. Phys.* **62**, 213–234 (1978).

44. Bott, R. & Seeley, R. Some remarks on paper of callias. *Commun. Math. Phys.* **62**, 235–245 (1978).
45. Hirayama, M. & Torii, T. fermion fractionalization and index theorem. *Prog. Theor. Phys.* **68**, 1354–1364 (1982).
46. Niemi, A. J. & Semenoff, G. W. fermion number fractionalization in quantum field theory. *Phys. Rep.* **135**, 99–193 (1986).
47. Lakes, R. Foam structures with a negative Poisson's ratio. *Science* **235**, 1038–1040 (1987).
48. Lawler, M. J. Emergent gauge dynamics of highly frustrated magnets. *New J. Phys.* **15**, 043043 (2013).

Acknowledgements

T.C.L. is grateful for the hospitality of the Newton Institute, where some of this work was carried out. This work was supported in part by a Simons Investigator award to C.L.K.

from the Simons Foundation and by the National Science Foundation under DMR-1104707 (T.C.L.) and DMR-0906175 (C.L.K.).

Author contributions

C.L.K. and T.C.L. contributed to the formulation of the problem, theoretical calculations, and the preparation of the manuscript.

Additional information

Supplementary information is available in the [online version of the paper](#). Reprints and permissions information is available online at www.nature.com/reprints. Correspondence and requests for materials should be addressed to T.C.L.

Competing financial interests

The authors declare no competing financial interests.